ORIGINAL ARTICLE

Numerical investigation on keyhole stability and weld pool dynamics during quasi-continuous laser beam welding of Ti6Al4V plate using constant and modulated high-frequency pulsed heat input

Jicheng Chen[1,2] · Xiaomei Chen[3] · Xuejun Liu[1,2] · Yanhong Wei[3]

Abstract

For numerical investigation of the quasi-continuous laser beam welding (Q-CLBW) process, the existing research usually considered a constant welding heat input, which to some degree loses accuracy in representing the welding dynamics. This paper developed a validated CFD model for the simulation of Q-CLBW of Ti6Al4V alloy based on a near-reality heat source model. The coupled transient temperature, velocity, and phase fields were solved under a high-frequency pulsed laser power (HF-PLP) at 5000 Hz as well as a constant laser power (CLP) which has been conventionally employed. Comparative analysis was carried out with respect to keyhole stability, melt flow pattern, and weld pool dimensions resulting from different heat sources and different heat input values with laser peak power of 2800~3800 W and welding velocity of 0.02~0.04 m/s. Results indicate that the time-dependent laser input yields less stabilized dynamics featured with middle-depth keyhole collapse, chaotic melt flow, and periodic vapor eruption, and such characteristics are difficult to be observed with CLP. The maximum temperature, pressure, and velocity magnitude of molten metal present remarkable oscillations in relation to welding time. With decreasing heat input in HF-PLP welding cases, the keyhole geometry tends to collapse in the tip segment while the melt flow becomes regular. Furthermore, the employment of the HF-PLP condition also enhances the accuracy in predicting the cross-sectional seam profile in terms of width and depth. Pulsed laser input should be taken into full consideration in the numerical simulation of the Q-CLBW process.

Keywords Quasi-continuous laser beam welding · High-frequency pulsed laser power · Constant laser power · Keyhole stability · Weld pool dynamics

1 Introduction

As a near-net-shape manufacturing process, quasi-continuous laser beam welding (Q-CLBW) has been widely concerned in automotive, aerospace, and aerospace industries because of its excellent performance in automatic production, material utilization, and product quality [1]. It has been prodigiously employed in the fabrication of light and green metals, including titanium and its alloys, to achieve improved strength-to-weight, energy conservation, and emission reduction [2].

Q-CLBW for titanium alloys evolves multi-phase and multi-physics coupling phenomena, typically the metal evaporation and keyhole effect, which leads to high complexity and nonlinearity in terms of thermal and flow behavior during the process. The keyhole stability determines the dynamic behavior of the molten pool to a great extent and ultimately affects the joint quality, including weld continuity, porosity rate, grain morphology, and mechanical properties.

The keyhole and molten pool dynamics occurring in the Q-CLBW process have been studied extensively through various experimental observation schemes. Seto et al. [3] examined the interrelationship between keyhole and plasma behavior by using a synchronous visualization system consisting of a high-speed camera and an X-ray transmission device.

✉ Yanhong Wei
  yhwei@nuaa.edu.cn

1   MIIT Key Laboratory of Pattern Analysis and Machine
    Intelligence, College of Computer Science and Technology,
    Nanjing University of Aeronautics and Astronautics,
    Nanjing 211106, China

2   Collaborative Innovation Center of Novel Software
    Technology and Industrialization, Nanjing 210023, China

3   College of Materials Science and Technology, Nanjing
    University of Aeronautics and Astronautics, Nanjing 211106,
    China

The effect of shielding gas flux on porosity formation mechanism in continuous wave CO_2 laser welding was investigated through simultaneous photography. Tao et al. [4] used a CMOS high-speed video system to observe the in-process weld pool dynamics during the welding process. To improve the image quality, a bandpass red laser with an emission wavelength of 808 nm was aligned as a backlight source to illuminate the welding zone. According to Wolff et al. [5], in situ X-ray imaging was employed to investigate the magnet-assisted weld pool and porosity evolutions in laser welding of 4140 steel. It was reported that a static magnetic field of 600 mT enables a less oscillated keyhole cavity, thus eliminating the porosities caused by keyhole collapse. Yi et al. [6] designed the "sandwich" assembly consisting of glass and base metal components side by side to capture the keyhole shape in the longitudinal section. A systematic study was made on the effects of Fresnel and inverse Bremsstrahlung absorptions on keyhole dynamics in CO_2 laser welding. Üstündağ et al. [7] recorded the keyhole morphology during high-power laser welding of a 25-mm-thick structural steel plate assisted by an alternating magnetic field. They showed that the induced electromagnetic stirring effect makes the keyhole profile deeper and the leading edge of the keyhole more inclined to the beam axis.

Computational fluid dynamics (CFD) simulation is a complementary tool that has been increasingly used in recent years to deal with in-process phenomena of Q-CLBW. The primary advantage of this approach is that the keyhole and weld pool behavior can be accurately and quantitatively reproduced from various physical perspectives, such as temperature, velocity vector, phase volume, and element fraction, based on customized numerical models. Ki et al. [8, 9] presented a self-consistent keyhole and multi-phase coupling model by using the level-set (LS) method. They performed the complete simulation of heat and mass transfer behavior, e.g., liquid–gas interface evolution, metal evaporation, Knudsen layer effect, and beam multi-reflections, during the deep-penetration CO_2 laser beam welding of steel sheets. Besides, the effects of laser power and scanning speed on keyhole profile, laser energy distribution, melt-flow velocity, and weld bead geometry were theoretically predicted and well verified. Another typical model proposed by Cho et al. [10, 11] simplified the gas/plasma as void and focused on single-phase problems during high-power laser welding. The volume-of-fluid (VOF) method was employed for free surface tracing under laser irradiation and recoil pressure. The molten pool dynamics coupling multiple physical factors were simulated, and the effects of beam profile, vapor shear force, and plume heating on the seam profile at cross-section were discussed. Pang et al. [12, 13] improved the LS method by introducing the particle correction strategy. It was revealed that the keyhole instability at different linear energies is closely related to the bulges on the keyhole wall. The simulation results also showed the periodic collapse

of keyhole and the formation of bubbles near the keyhole tip. Moreover, the dynamics of metallic vapor, including local evaporation, plume swing, and gas entrapment were investigated using a multi-time scale approach. Luo et al. [14] explored the keyhole and weld pool behavior during underwater laser welding. The numerical results indicated that with the increasing water pressure, the average temperature at the keyhole surface increases while the keyhole depth reduces due to the higher boiling point. As with water cooling, Marangoni convection near the weld pool surface is almost eliminated due to the rapid solidification rate. Li et al. [15] carried out numerical and experimental research on quasi-continuous laser welding of Ti6Al4V alloy plates with different thicknesses and showed that the heat-affected zone and molten pool can be diverted to the thinner sheet side. Yang et al. [16] modeled and investigated the physical phenomena during the double-sided laser welding of the t-shaped joint of aluminum alloy. It was found that the variation trend of porosity defects is closely related to the keyhole state and melt flow pattern.

In the numerical study of Q-CLBW, most numerical models adopt a continuous heat source, namely, a constant laser power (CLP) input. Nevertheless, this process is actually implemented by utilizing a high-frequency pulsed laser beam (HF-PLP) (10^3~10^6 Hz), according to Chen et al. [17]. Under the intermittent laser power, the keyhole and weld pool would exhibit very different characteristics in temperature, velocity, and geometry, compared to the numerical results with CLP.

At present, heat source modeling based on pulse waveform is mainly applied to pulsed laser beam welding (PLBW) with low and medium pulse frequency. Kumar [18] modeled the heat source with a rectangular waveform for the simulation of PLBW of 316L stainless steel. The transient thermal response across and temperature field was analyzed at a pulse frequency of 20 Hz and pulse width of 12 ms. Li et al. [15] exploited a pulsed 2D Gaussian laser heat source to investigate the thermal process in laser welding of Ti6Al4V sheets at different thicknesses. Comparative analysis was performed on thermal cycle curves resulting from different focus lengths, laser speeds, and laser powers. Zhou et al. [19, 20] simulated the keyhole dynamics in PLBW of 304 stainless steel and pointed out that the keyhole collapse and porosity formation occurring during the pulse interval is caused by the downward refilling of liquid metal lagging behind the solidification of the molten pool. By introducing an external electromagnetic support system, the filling rate is improved and porosity prevention is realized numerically and experimentally. Liang and Luo [21] simulated the surface deformation of Ti6Al4V-Niobium dissimilar joint prepared by a 10~20 Hz pulsed laser beam, based on the local drilling velocity model coupled with Gaussian heat source at the workpiece surface. It showed that the higher pulse

overlap coefficient reduces the solidification rate and makes the penetration fluctuation smaller and surface ripples finer. Chen et al. [22] employed a 20 Hz pulsed laser beam to weld 2 mm-thick Ti6Al4V sheets assembled in butt joint configuration with a reserved air gap. The gap bridging dynamics, as well as the beam formation, was numerically investigated and experimentally validated. The gap size accounting for 16.67% of base metal thickness is permitted for a desirable welding formation, indicating that the assembly tolerance was effectively improved compared to the data reported in Salminen [23].

To reproduce the heat and flow behavior of molten pool during the Q-CLBW process and enhance the reliability of the prediction results, in the current research, an improved numerical model was developed by taking the high-frequency pulsed characteristic of the laser beam into account. Simulations were conducted on autonomous welding of Ti6Al4V plates under various heat input values. The temperature, velocity, and phase fields were calculated using practical HF-PLP and pure CLP, respectively. Comparative analysis and discussion were performed on keyhole stability, melt flow pattern, and weld pool dimensions corresponding to the laser input conditions. The necessity of considering a time-dependent laser power in Q-CLBW simulation was primarily evaluated.

2 Experiment

As demonstrated in Fig. 1, the bead-on-plate Q-CLBW process was performed on a Ti6Al4V workpiece sized 100 mm × 100 mm × 5.6 mm. The laser device employed is *Trudisc 4001* (made by *TRUMPF China Co. Ltd.* in Taicang, China) which possesses adjustable output power of 80~4000 W, a wavelength of 1030 nm, and a beam parameter production (BPP) of 4 mm·mard. The initial incident beam was set vertical to the plate surface with zero
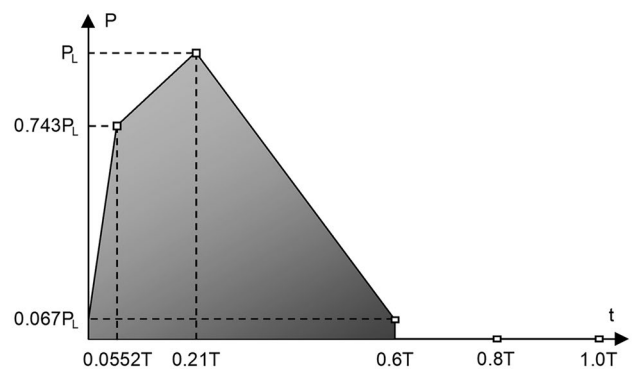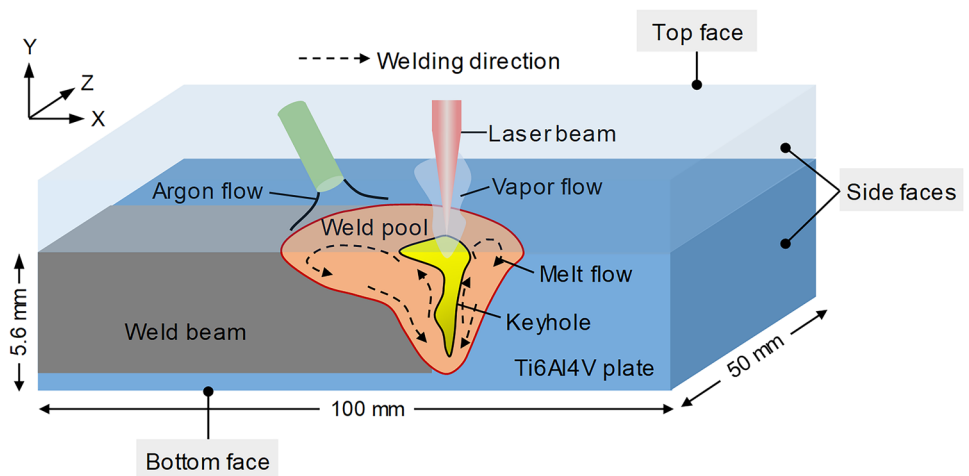
Fig. 2 Laser waveform applied for Q-CLBW experiment

defocusing amount. During the welding, a unilateral shielding argon flux at 20 L/min was provided to the upper surface of the workpiece.

The modulated laser waveform, namely the laser power-time curve employed for Q-CLBW experiments is shown in Fig. 2. It has two ramp-up stages and one ramp-down stage, which benefit a lower thermal crack risk compared to a square or step pulse shaping [24].

As expressed in Eq. (1), a novel formula is developed for the averaged heat input calculation in each pulse period with respect to arbitrary pulse waves employed.

$$q_p = \frac{\eta_0 P_L \int_0^{T_p} k_P(t)dt}{u_0 T_p} \tag{1}$$

Here, η_0, P_L, T_p, and u_0 denote heat efficiency, laser peak power, pulse period, and welding speed. $k_P(t)$ is the time-dependent laser power percentage in each pulse period. For square waves, when the initial phase is zero, the formula has the following form:

$$q_p = \frac{\eta_0 P_L r_p}{u_0} \tag{2}$$

Fig. 1 Schematic description of CLBW of Ti6Al4V plate

which is consistent with Gao et al. [25] with r_p being the duty ratio.

The critical welding processing parameters are shown in Table 1. The heat efficiency of laser welding is commonly defined as 0.9. The heat input at five levels is designed by changing the laser peak power and the welding speed.

The weld beams were then processed with wire cutting, mounting, polishing, and acid etching with Kroll reagent ($8\% \text{ HNO}_3 + 2\% \text{ HF} + 90\% \text{H}_2\text{O}$ in *wt.*) for metallographic examination. The cross-sectional morphology was captured by optical microscopy *MR-5000* (made by *Jiangnan Yongxin Optics Co. Ltd.* in Nanjing, China).

3 Numerical model

A multi-phase flow model based on the assumptions of incompressible, laminar, and non-isothermal immiscible is developed. Fundamentally, the conservations of mass, momentum, and energy take the following forms.

$$\nabla \cdot \mathbf{u} = 0 \tag{3}$$

$$\rho \left(\frac{\partial \mathbf{u}}{\partial t} + (\mathbf{u} \cdot \nabla)\mathbf{u} \right) = \mu_l \nabla \cdot \left[\nabla \mathbf{u} + (\nabla \mathbf{u})^T \right] - \nabla p - \mathbf{S}_M \tag{4}$$

$$\frac{\partial}{\partial t}(\rho H) + \nabla \cdot (\rho H \mathbf{u}) = \nabla \cdot (k \nabla T) + S_E \tag{5}$$

Here, $\mathbf{u}$, ρ, μ_l, p, t, S_M, H, k, T, and S_E denote velocity vector, mass density, dynamic viscosity, fluid pressure, physical time, momentum source term, mixing enthalpy, thermal conductivity, temperature, and energy source term, respectively.

Basically, the liquid and gas phases consisting of the computational domain are subjected to the gravity $\mathbf{f_g}$ and the thermal buoyancy $\mathbf{f_b}$. For the calculation of the melting-solidification process, the enthalpy-porosity relation and Darcy resistance $\mathbf{f_D}$ are employed to handle the momentum attenuation in the solid-liquid mixture. With the weld pool being rapidly heated to or over the evaporation point, the recoil pressure $\mathbf{f_r}$ is calculated and applied to the liquid surface. The momentum source term $\mathbf{S}_M$ reads

$$\mathbf{S}_M = -\rho \mathbf{g} + \rho \mathbf{g}\beta(T - T_0) - K_0 \frac{(1-\alpha_l)^2}{\alpha_l^3 + c}(\mathbf{u} - \mathbf{u}_0) + \frac{AB_0}{\sqrt{T}} \exp\left(\frac{-M_a H_v}{N_a k_b T}\right) \cdot \mathbf{n} \tag{6}$$

Here, $\mathbf{g}$, α_l, $\mathbf{u}_0$, β, and T_0 are gravitational acceleration, liquid volume fraction, initial velocity field, thermal expansion coefficient, and ambient temperature. K_0 and c are Darcy resistance coefficients, respectively. A, B_0, M_a, H_v, N_a, and k_b are pressured-related coefficients, evaporation constant, molar mass, evaporation latent heat, Avogadro constant, and Boltzmann constant, respectively. $\mathbf{n}$ is the normal unit vector of the free interface pointing to the liquid phase side.

Considering the weak ionization of metallic vapor with a disc laser, the plasma phase, as well as the inverse bremsstrahlung effect, can be ignored [26]. The energy source term S_E contains the Rayleigh scattering absorption Q_R, Fresnel absorption Q_F, and surface heating effect Q_s due to the vapor eruption.

$$S_E = Q_R + Q_F + Q_s \tag{7}$$

As illustrated in Fig. 3, the initial incident of the laser beam is set vertically to the workpiece surface. The beam spot shrinks spatially with a decreasing radius from the initial r_b to the focused r_f, following the practical BPP of the laser. The beam spot extracted with a radius of r_0 is uniformly discretized into a bunch of sub-beams (the blue cells), carrying power densities corresponding to Gaussian distribution approximation [27]:

$$q(r) = \frac{3\eta_0 P(t)}{\pi r_0^2} \exp\left(\frac{-3r^2}{r_0^2}\right) \tag{8}$$

where $P(t)$ is time-dependent laser power and r is the distance from the arbitrary cell center node to the spot circle center.

As described in Eq. (9), the Rayleigh scattering is calculated when the sub-beams travel through the metallic vapor, which causes the heating of vapor phase and the attenuation of laser power density [22]. The Fresnel absorption is calculated where the sub-beams intersect the liquid–gas interface, as depicted in Eq. (10) [28].

Table 1 Experiment cases and processing parameter sets

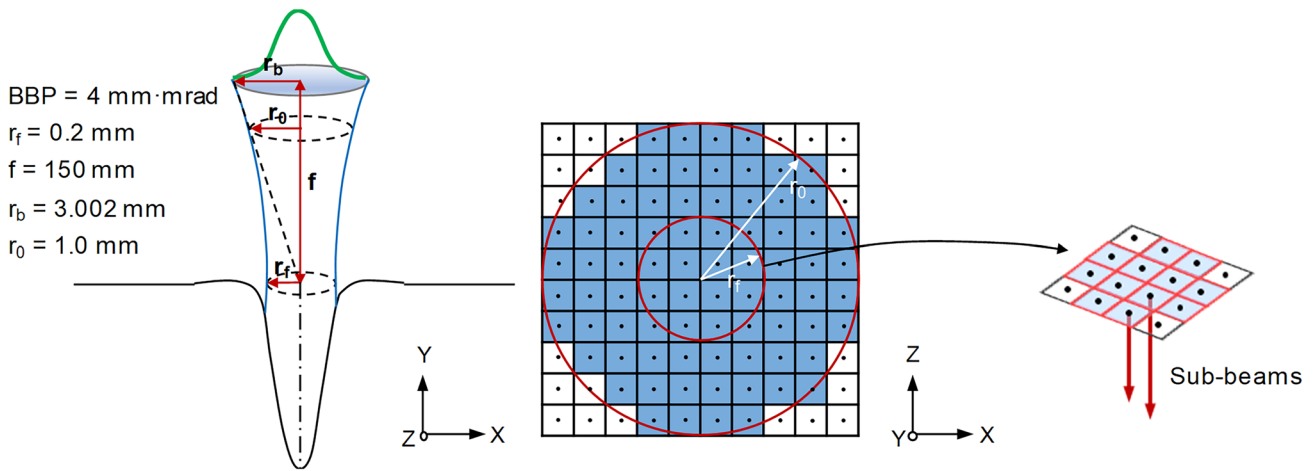| Case no.	Laser peak power P_L (W)	Welding speed u_0 (m/s)	Pulse frequency f_p (Hz)	Duty ratio r_p	Heat input on average q_p (J/mm)
#1	3800	0.02	5010	0.6	62.47
#2	3300	0.02	5010	0.6	53.25
#3	2800	0.02	5010	0.6	46.03
#4	3800	0.03	5010	0.6	41.65
#5	3800	0.04	5010	0.6	31.23

Fig. 3 Optical parameters of laser beam and beam discretization method

Multi-reflection of the beam inside the keyhole is handed by mirror reflection relation, as expressed in Eq. (11).

$$Q_R = \sum_{n=1}^{bn} \sum_{m=1}^{mr} q_{m-1,n}(r)\left(1 - \exp\left(\int_{lm-1}^{lm} \alpha_R dl\right)\right) \quad (9)$$

$$Q_F = \sum_{n=1}^{bn} \sum_{m=1}^{mr} q_{m-1,n}(r)\exp\left(-\int_{lm-1}^{lm} K_{pl} dl\right)\left(\mathbf{I}_m \cdot \mathbf{n}_m\right) \cdot \alpha_{F,m}(\theta_m) \quad (10)$$

$$\mathbf{R} = \mathbf{I} + 2(-\mathbf{I} \cdot \mathbf{n})\mathbf{n} \quad (11)$$

Here, q, α_R, l, and θ are laser power density during travelling, Rayleigh scattering coefficient, beam forward distance, and reflection angle. m numbers the multi-reflection time from 1 to mr, while n numbers the sub-beams from 1 to bn. α_F is the Fresnel absorption coefficient following the Hagen-Rubens relation:

$$\alpha_F(\theta) = 1 - \frac{1 + (1 - \varepsilon\cos\theta)^2}{2 + 2(1 + \varepsilon\cos\theta)^2} - \frac{\varepsilon - 2\varepsilon\cos\theta + 2\cos^2\theta}{2\varepsilon + 4\varepsilon\cos\theta + 4\cos^2\theta} \quad (12)$$

with ε being a material constant related to its electrical conductivity.

When the temperature at the liquid surface exceeds the evaporation point, the classic LEE model [29] is employed to deal with the liquid–gas mass transfer along with the latent heat. Furthermore, the vapor heating around the keyhole opening can be implemented by employing a Gaussian surface heat source, as suggested by Norman et al. [30]:

$$Q_s(r) = \frac{3\eta_1 P(t)}{\pi r_s^2} \exp\left(\frac{-3r^2}{r_s^2}\right) \quad (13)$$

with η_1 and r_s being vapor heating efficiency and radius of heat source.

The THINC/LS algorithm [31], which integrates high-order accuracy and strict mass conservation is used to track the liquid-gas interface. The basic equations can be expressed as:

$$\phi(\mathbf{x}, t) = \begin{cases} \text{dist}(\mathbf{x}, \partial V) & \mathbf{x} \in V^1 \\ 0 & \mathbf{x} \in \partial V \\ -\text{dist}(\mathbf{x}, \partial V) & \mathbf{x} \in V^2 \end{cases} \quad (14)$$

$$H(\mathbf{x}, t) = \frac{1}{2}\left[1 + \tanh\left(\overline{\beta}\phi(\mathbf{x}, t)\right)\right] \quad (15)$$

Here, Eq. (14) is the signed distance function where $\mathbf{x}$ is the arbitrary coordinate within the fluid domain, and V^1, V^2, and ∂V denote the liquid phase, gas phase, and interface zones. Equation (15) is the hyperbolic tangent function which is reconstructed by using a grid-related constant, $\overline{\beta}$, and the signed distance function to meet a range of (0, 1).

The geometry evolution of the phase interface is dominated by the transportation equations of LS and THINC variables, which read

$$\frac{\partial \phi}{\partial t} + \mathbf{u} \cdot \nabla\phi = 0 \quad (16)$$

$$\frac{\partial H}{\partial t} + \nabla \cdot (\mathbf{u}H) = 0 \quad (17)$$

The computational domain is locally extracted from the workpiece with a length of 5.6 mm, a width of 5.6 mm, and a height of 6.4 mm (thickness). The geometry is uniformly dispersed with uniform cube elements sized

Table 2 Initial and boundary conditions of domain for numerical solution

Condition	Thread	Energy	Momentum
Initial	Cells	$T_0 = T_\infty$	$\vec{u}_0 = 0$
Boundary	Top face	Adiabatic	$p_{gauge} = 0$
	Bottom face	Mixed convection and radiation [12]	$\vec{u}_{wall} = 0$
	Side faces of Ti6Al4V	Continuum [32]	$\vec{u}_{wall} = 0$
	Side faces of argon	Adiabatic	$p_{gauge} = 0$

0.8 mm and then is initialized to a liquid region (5.6 mm at thickness) and a gas region right above the liquid. The initial and boundary conditions of cell and face are classified in Fig. 1, and defined mathematically in Table 2 in terms of energy and momentum.

The thermophysical properties of Ti6Al4V and argon which respectively occupy the initial liquid and gas regions of domain are consistent with our previous research [17], as listed in Table 3.

The material property of the cells at the liquid–gas interface can be calculated by [17]:

$$\zeta_{interface} = \zeta_l H(\phi) + \zeta_g (1 - H(\phi)) \tag{18}$$

with ζ_l and ζ_g being the properties of liquid phase and gas phase.

4 Results and discussion

4.1 Simulation implementation and results verification

The proposed model is solved using a CFD platform *ANSYS Fluent 18.0*. The realistic simulation of the Q-CLBW process is performed based on the consideration of HF-PLP.

The pulse frequency applied is slightly modified to 5000 Hz to facilitate the result extraction. To achieve comparative analysis and accuracy evaluation, the conventional numerical scheme is also presented by using a CLP, which equals the peak value of HF-PLP. The other process-related parameters in both cases follow Table 1. The solution time is set 70 ms covering 140 pulse cycles with a time step of 0.001 ms.

The weld pool morphologies corresponding to cases #1, #3, and #5 under the function of HF-PLP were calculated and compared with the experimental results. As shown in Fig. 4, a sound symmetry is always achieved between the fusion line of seam and the solidus line of weld pool with the increase of the averaged heat input applied. According to the measurement at the cross-section, the averaged deviations of weld depth (WD) and half-weld width (H-WW) are 1.83% and 2.35%, respectively. The high precision prediction of weld morphology preliminarily confirms the rationality and accuracy of the model coupled with pulsed-mode heat input.

4.2 Keyhole and weld pool dynamics in CLP and HF-PLP welding cases with equal laser peak power

Figure 5 summarizes the calculated temperature and phase fields during the keyhole penetrating period under CLP and HF-PLP conditions. The as-built weld pool region is highlighted with solid black lines, and is colored using a localized temperature legend of 400~3000 K. As can be seen, with a constant laser input, the keyhole profile is in an inverted-conical shape surrounded by a thin layer of liquid metal. The keyhole wall presents slight fluctuation in terms of topological morphology and temperature distribution due to the dynamic instability [10, 12]. In contrast, the keyhole profile is more fluctuated when high-pulsed laser power is employed, especially near the tip section. The temperature at the keyhole wall decreases obviously as the welding proceeds from 6.042 to 6.2 ms, corresponding to the laser power percentage decreasing from 100% to zero.
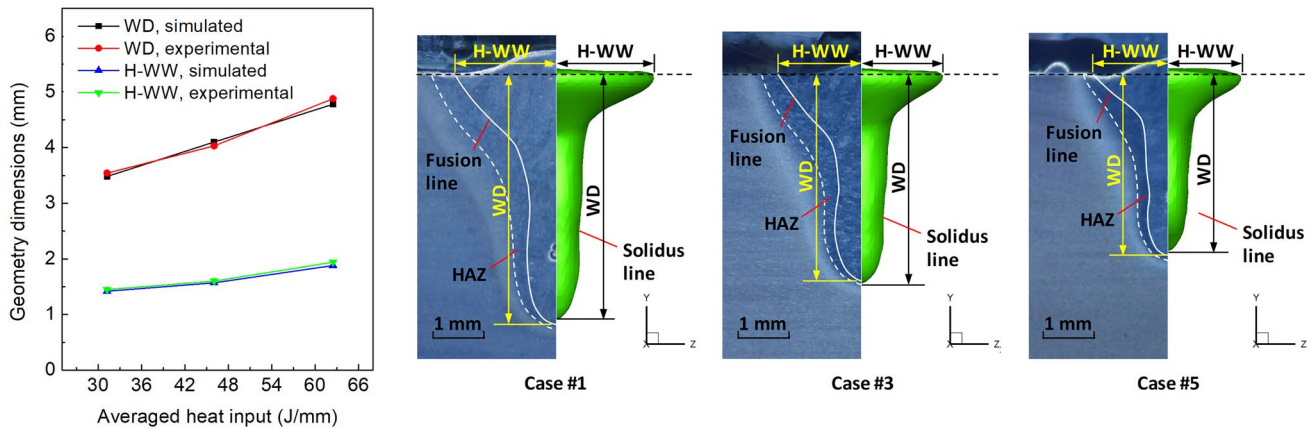
Table 3 Thermophysical properties of Ti6Al4V titanium alloy and argon

Thermal-physical property	Symbol	Ti6Al4V	Argon	Unit
Density	ρ	8190	1.6228	kg/m^3
Thermal expansion coefficient	β	1.1×10^{-5}		
Solidus temperature	T_l	1533		K
Liquidus temperature	T_s	1609		K
Evaporation point	T_v	2917		K
Specific heat	C_p	435 at T_0, 723 at T_l	520.64	J/(kg·K)
Heat conductivity (T_0)	λ	8.9 at T_0, 29.6 at T_l	0.0158	W/(m·K)
Latent heat of fusion	L_m	2.1×10^5		J
Latent heat of evaporation	L_v	6.09×10^6		J
Dynamic viscosity	η	8.89×10^{-3}	2.125×10^{-5}	Pa·s
Surface tension coefficient	σ	1.893		N/m
Marangoni coefficient	$\partial_\sigma / \partial T$	-1.1×10^{-4}		N/(m·K)

Fig. 4 The simulated seam profile and dimensions in comparison to the experiment results

Due to the imbalance between surface tension and recoil pressure, the keyhole geometry shrinks in volume and then collapses in the tip segment at the end of the pulse period.

As the numerical process progresses to ~52 ms, the keyhole geometry has a full growth indicating that the welding dynamic behavior approaches the quasi-steady state. As shown in Fig. 6, in the welding case with CLP, small porosity caused by keyhole collapsing can be observed at the bottom of the weld pool. When HF-PLP is applied, the middle and lower segments of the keyhole become slenderer due to the reduction of heat input, according to Eq. (1). Moreover, with the decreasing laser power, the temperature at the keyhole surface shows an overall drop, and several contraction shapes appear on the keyhole surface. The collapsing occurs at the middle penetration during the pulse interval, resulting in a sharp decrease of keyhole depth as well as a prominent irregular porosity.
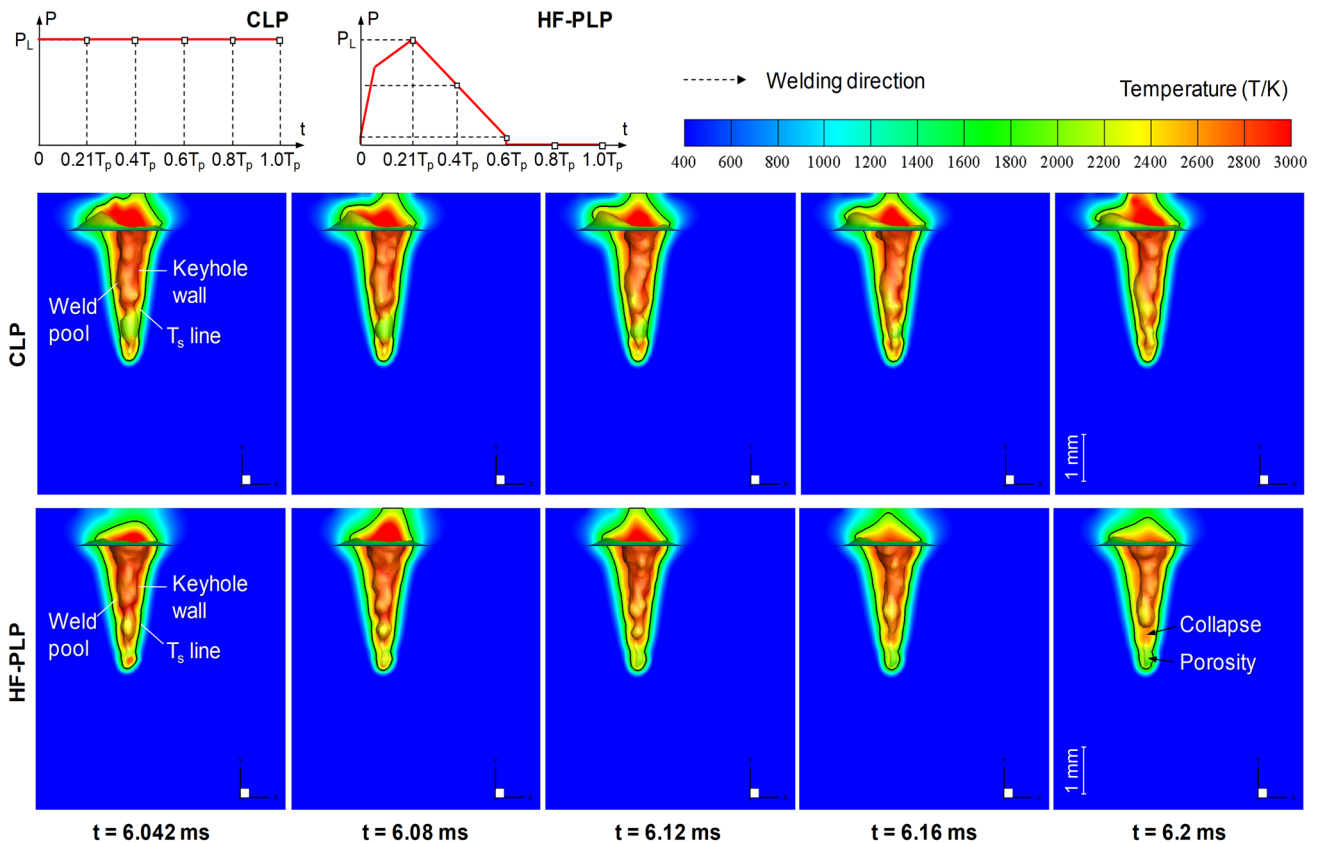
Fig. 5 Comparison of temperature and phase fields resulted from CLP and HF-PLP conditions during keyhole growing stage
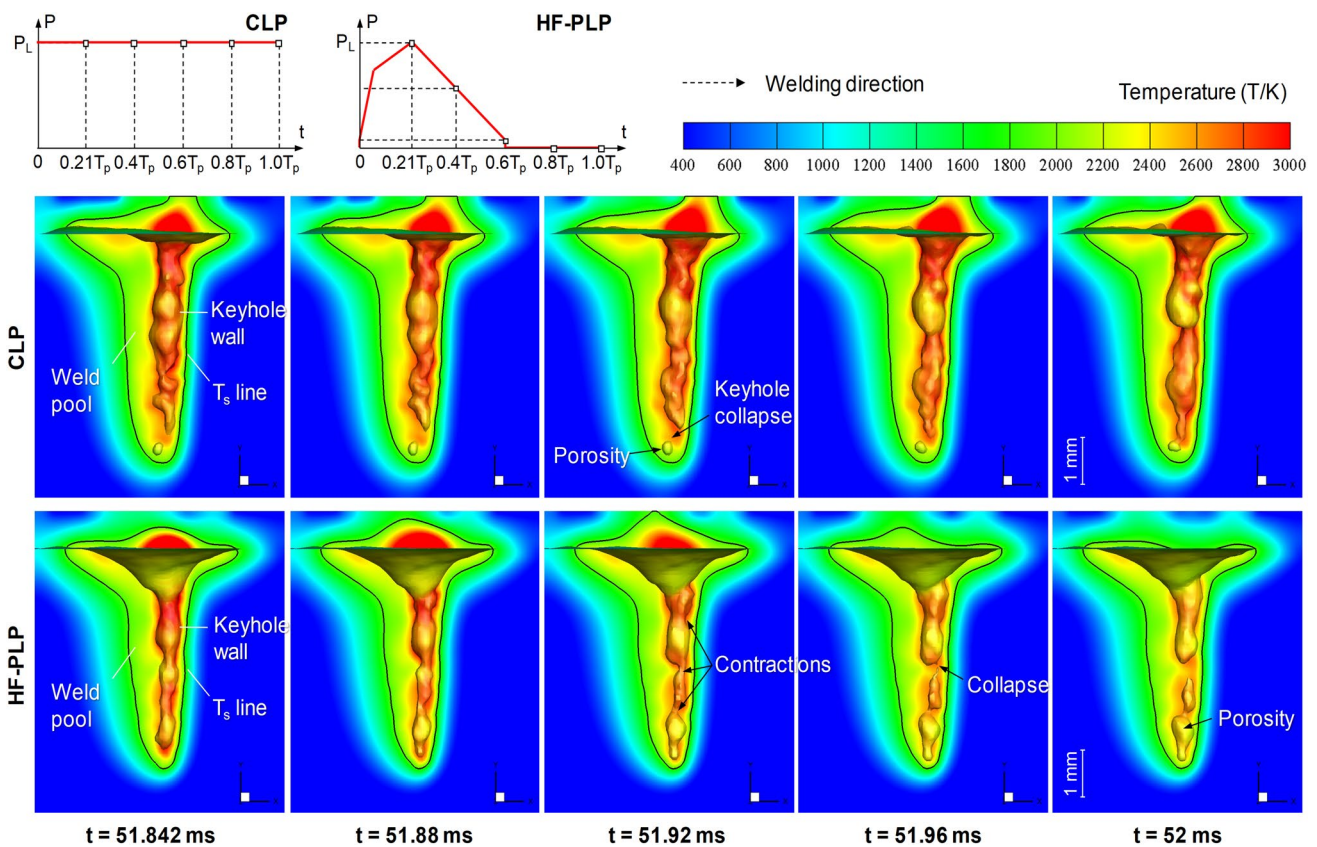
Fig. 6 Comparison of temperature and phase fields resulted from CLP and HF-PLP conditions during quasi-steady-state stage

Furthermore, on a larger time interval scale within 70 ms, it can be observed that the keyhole collapses more remarkably and frequently in the HF-PLP condition than in the CLP condition, as can be seen in Fig. 7. Under the intermittent laser input, the middle-depth collapse occurs at both growing and fully developed stages of the keyhole, leading to an average reduction of 14.04% in keyhole depth compared with the data measured with constant laser input, as presented in Fig. 8.

In Figs. 9 and 10, the transient velocity field which consists of the melt flow inside the weld pool and the vapor flow outside the keyhole wall is presented in combination with the keyhole profile. Two scales are used to eliminate the mapping problem caused by the difference of magnitude between gas and liquid velocity values, wherein the vapor flow follows the vector scale while the melt flow vectors are homogenized and colored by the contour legend.

The subpictures exhibited in Fig. 9 show that the gas eruption intensity during the welding with HF-PLP decreases obviously after the laser shuts down at 6.12 ms, while that in CLP welding is almost unchanged. This indicates that the local temperature of the keyhole wall can be kept above the boiling point to maintain liquid evaporation during the keyhole growth stage.

Figure 10 records the fluid velocity field of the keyhole and molten pool with fully developed geometry as the welding process exceeds 50 ms. Similar to the numerical reports in the pieces of literature [8–13], the thermal-capillary convection featuring with an anticlockwise vortex is induced near the upper surface of the weld pool. Besides, local velocity spikes (depicted by red arrows) can be observed around the necking segments of the keyhole, since the presence of the local bulges reduces the laser propagation distance and thus enhances the Fresnel absorption as well recoil pressure levels. As the laser power decreases in the HF-PLP case, the impact of surface tension on molten metal flow becomes dominant near the gas-liquid interface, leading to backfilling of melt towards the interface contractions which cause the continuous necking and finally keyhole collapsing. In addition, compared with Fig. 9, the intensity of Rayleigh scattering absorption enhances with the deepening of the keyhole, and the remarkably cooled keyhole wall cannot sustain the evaporation of liquid metal. Therefore, the vapor eruption character above the keyhole opening disappears, as demonstrated in the subpicture of 52 ms.

In Fig. 11, the maximum temperature, pressure, and velocity values of liquid phase within 2 ms (covering 10 pulse periods in HF-PLP welding cases) are measured and depicted in relation to welding time.
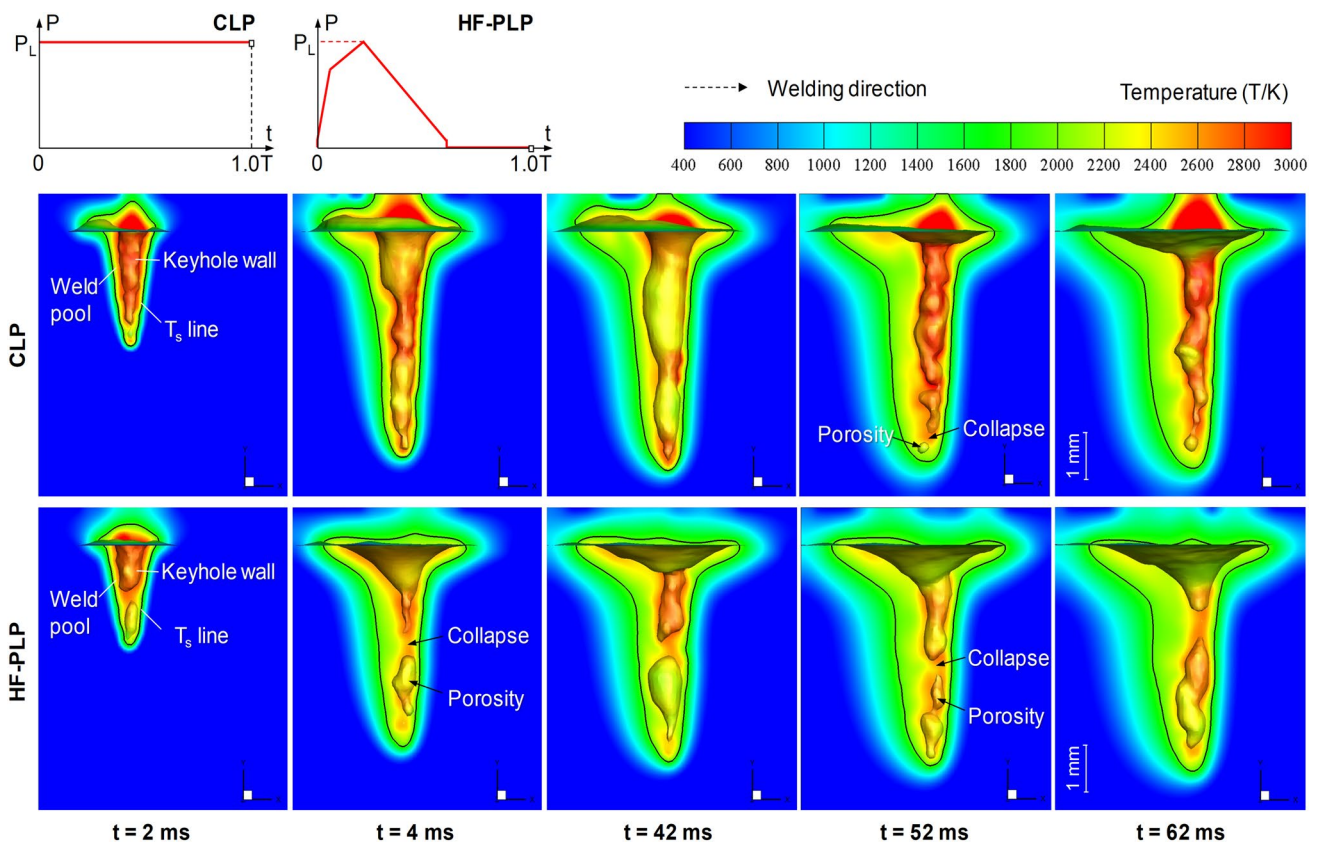
Fig. 7 Comparison of temperature and phase fields resulted from CLP and HF-PLP conditions at certain moments

Basically, the target measurement positions locate in gas-liquid coexistence area. The maximum temperature values resulting from a constant laser power are between the boiling point T_v and 500 K above T_v, consistent with the numerical data reported in [10, 33]. The curve oscillation is fundamentally attributed to the evolution of the keyhole front-wall morphology lagging behind the advance of the laser spot, which changes the primary reflection angle
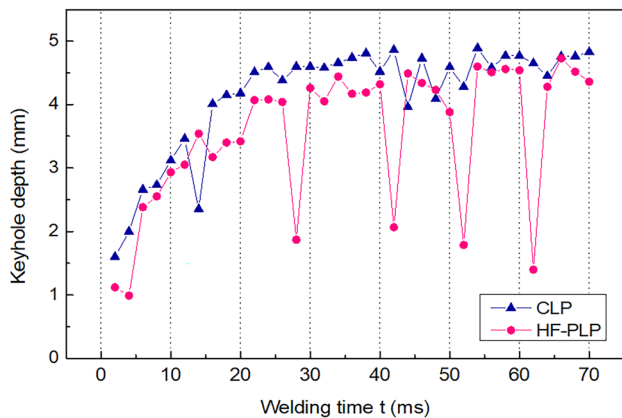
Fig. 8 Measurement of keyhole depth with the time interval of 10 ms

of the laser beam and accordingly the Fresnel absorption coefficient, according to Eq. (10). Moreover, the Rayleigh scattering effect also affects the temperature of the keyhole wall, depending on the thickness of the gas phase between the initial position of the laser spot and the beam-keyhole intersection point [34]. Therefore, the higher temperature peaks occurring in 51.6~51.8 ms are probably due to the decline of keyhole depth caused by tip-mode collapse, as presented in Fig. 11a. In Fig. 11b, the maximum temperature–time curve has distinctive oscillation characteristics wherein the major oscillation period (MOP) is basically consistent with the laser pulse period while the major oscillation amplitude (MOA) is much larger than that in the CLP case. Besides, the valley values can be lower than T_v at the end of each pulse cycle. This is an indicator that the significant keyhole collapse occurs during the measured pulse periods, that is, the necking and collapsing appear at relatively high positions along the Y-axis, leading to the weakened Rayleigh scattering effect as well enhanced Fresnel absorption flux.

As shown in Fig. 11c, d, the maximum pressure of molten metal is highly correlated to the maximum temperature especially in two laser irradiation conditions with the abscissa interval between the adjacent peaks close to one pulse
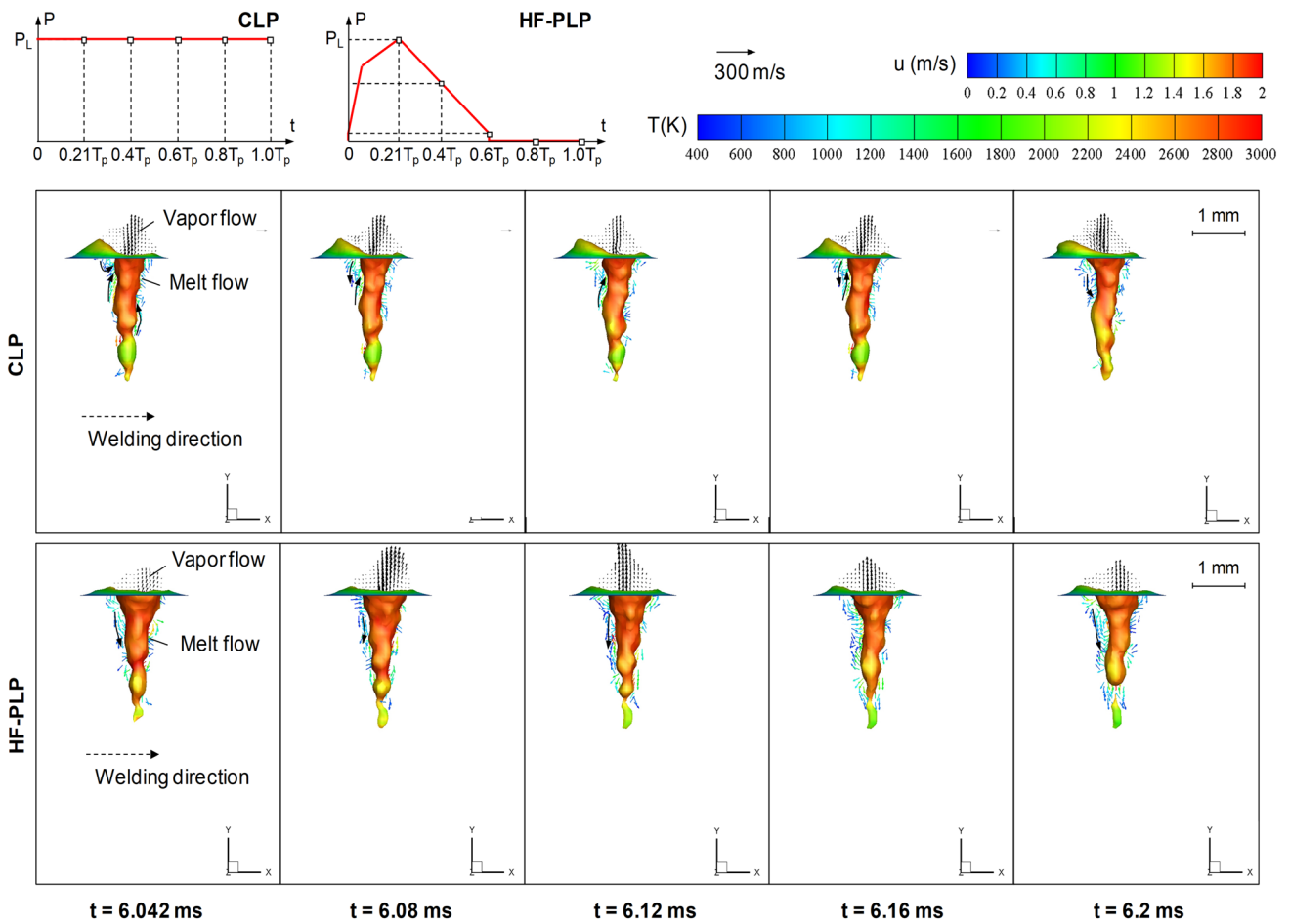
Fig. 9 Comparison of velocity field resulted from CLP and HF-PLP conditions during keyhole growing stage

period, indicating that the temperature-dependent recoil pressure dominates the momentum source terms during the welding process. However, the velocity curve shown in Fig. 11f is less related to the temperature curves in terms of MOP and MOA.

To explore further, the melt flowing mechanism, as well as the velocity variation principle under the action of momentum factors, is schematically depicted in Fig. 12a. It is known that the higher temperature simultaneously increases the local gradient of surface tension and in turn the Marangoni shear force which promotes the melt flowing (Marangoni flow) along the tangential vectors of the keyhole wall [30]. This momentum factor can be expressed by Eq. (19) with γ being the surface tension coefficient. Then, the current velocity vector u_1 driven by the resultant force of recoil pressure and Marangoni shear force could be enhanced or weakened, largely depending on the temperature gradient at the position of liquid phase at t_1 moment, as depicted in Fig. 12b. Therefore, the maximum

velocity of molten metal and its occurrence moment have certain randomness in each pulse period, which can be responsible for the poor correlation to the maximum temperature distributions.

$$\tau_M = \frac{\partial \gamma}{\partial T} \nabla_s T \tag{19}$$

4.3 Keyhole and weld pool dynamics in CLP and HF-PLP welding cases under various heat input

In this subsection, the numerical simulations based on continuous and high-frequency pulsed laser power are subjected to various heat input values by changing the laser peak power P_L and the welding speed u. The calculated temperature, velocity vectors, and phase distributions within 2 ms at the quasi-steady-state stage are presented in Figs. 13, 14, 15 and 16.
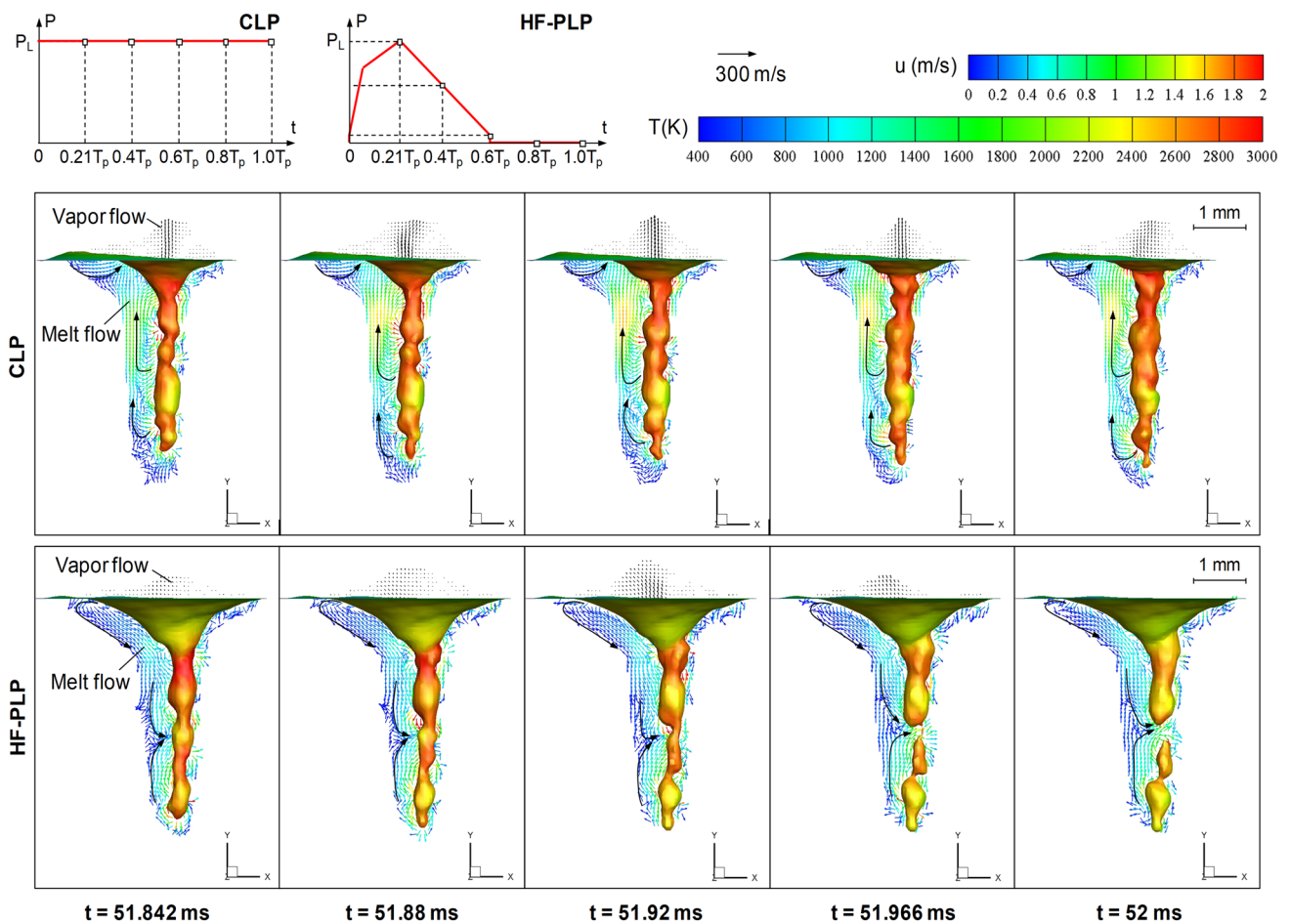
Fig. 10 Comparison of velocity field resulted from CLP and HF-PLP conditions during quasi-steady-state stage

As demonstrated in Fig. 13 corresponding to the CLP welding process, the keyhole and the weld pool plotted in the symmetry plane show dimensional reductions in length and depth, with the constant laser power decreasing from 3300 to 2800 W. The keyhole surface becomes smoother with fewer bosses and contractions, and the molten metal around the keyhole is decelerated resulting in a relatively regular flow pattern with uniform velocity distribution within the weld pool. The geometrical collapsing tendency at the keyhole tip decreases reflecting that the dynamic stability is improved, which agrees well with Ahh et al. [35]. Moreover, the lower heat input cools the keyhole surface and hence reduces the evaporation rate of liquid metal, which can be addressed from the shorter vapor eruption vectors under the same scale. As observed by reducing the laser power, similar physical phenomena including the smaller keyhole penetration and

the stabilized melt dynamics are obtained as the welding speed reduces from 0.02 to 0.04 m/s. Besides, the leading edge of keyhole becomes more slant with a vertical angle increasing from 2.69 to 5.46°, reproducing the Q-CLBW process numerically conducted on aluminum and austenite stainless steel [12, 36]. It is mainly because the positions of first Fresnel absorption move upward with the increase of welding speed, and in turn, the keyhole interface can be more heated and firstly recoiled in the upper part, according to Tan and Shin [37]. Apart from the inclined keyhole profile, the gradually enhanced vapor eruption intensity can be found with higher welding speeds applied, which is mainly attributed to the attenuated Rayleigh scattering effect before the first Fresnel absorption.

As presented in Fig. 14, in general, as the heat input varies, the thermal-flow behavior as well as the keyhole evolution simulated in HF-PLP condition is still
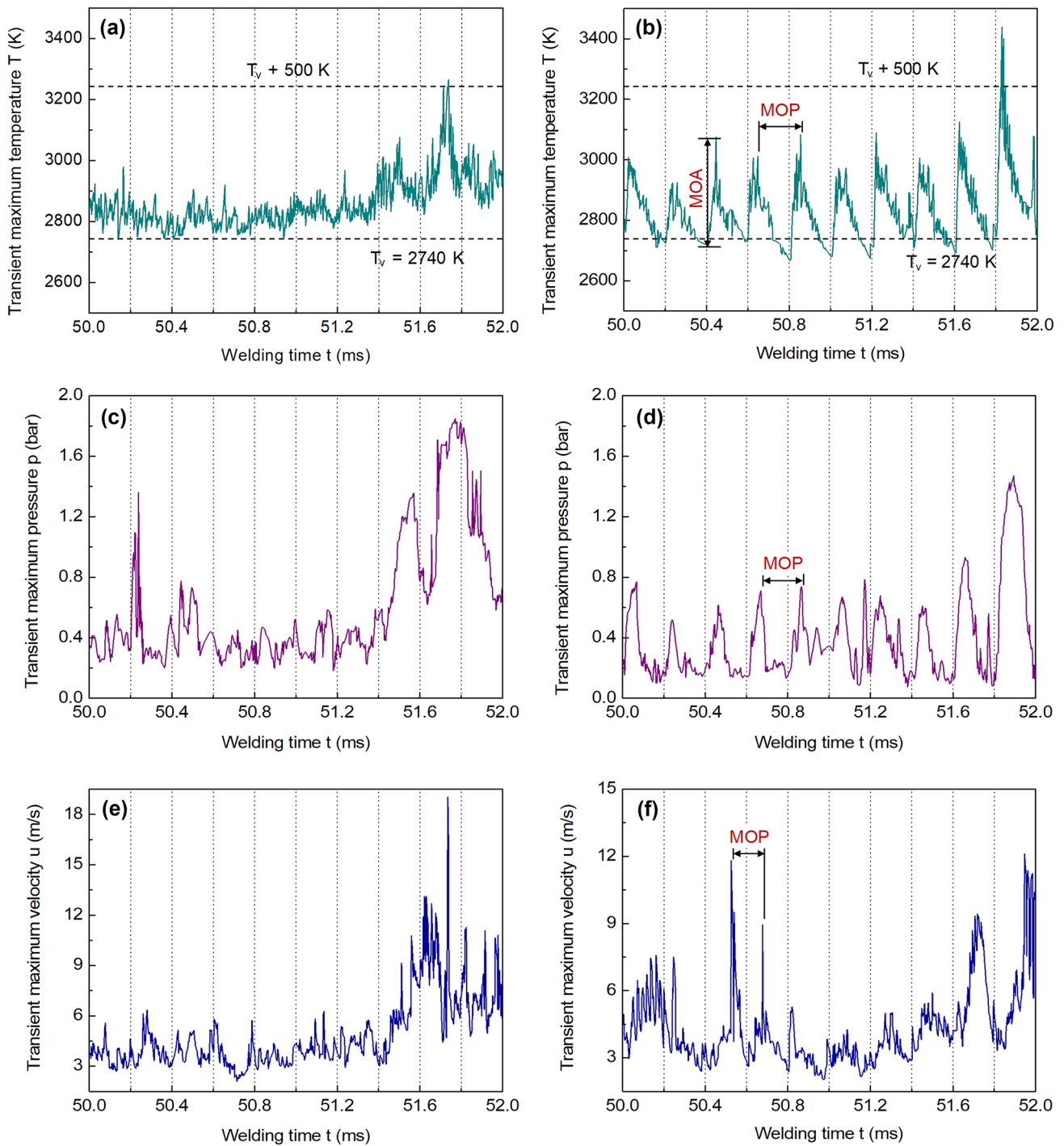
Fig. 11 Measurement of maximum temperature, pressure, and velocity values in liquid phase in relation to welding time. **a** Temperature–time curves in CLP case; **b** temperature-time curves in HF-PLP case; **c** pressure-time curves in CLP case; **d** pressure-time curves in HF-PLP case; **e** velocity magnitude-time curves in CLP case; **f** velocity magnitude-time curves in HF-PLP case

Fig. 12 Melt flowing mechanism and velocity variation under the action of momentum factors. **a** Micro melt at t_0; **b** Micro melt at t_1
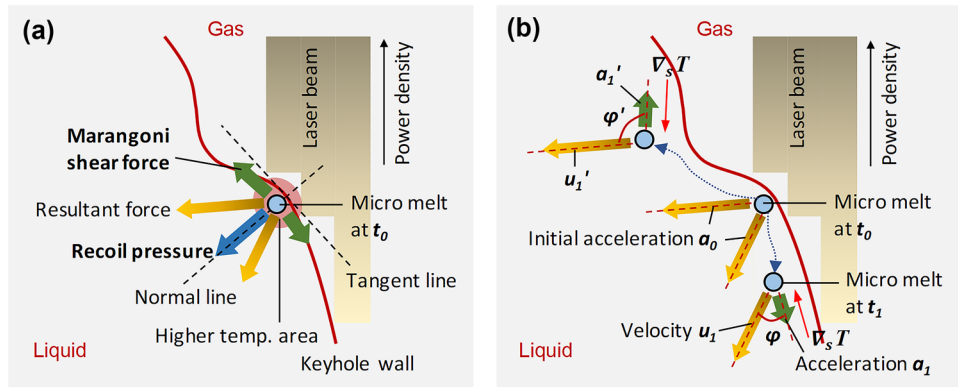
quite different from that of CLP condition. According to Fig. 15, the application of lower laser peak powers facilitates the elimination of keyhole collapse and the resultant porosity, wherein the keyhole profile tends to shrink and rebound as a whole. The discrepancy is that the necking position of the keyhole in pulsed welding cases is relatively random, and the keyhole morphology preserved during the previous pulse interval would yield a significant impact on the dynamic and geometrical evolutions in the current pulse period. Therefore, although the collapse is eliminated, the keyhole topology can have more fluctuation as laser peak power further declines from 3300 to 2800 W. The compensation flows can be notable near the trailing edge of the keyhole, as seen in Fig. 16. The attenuation of vapor flow intensity caused by the reduced laser peak power can also be noticed in periodic vapor eruptions. The decrease in welding velocity decelerates the melt flow and reduces the keyhole depth at the fully developed stage. Similarly, the collapse risk of keyhole geometry with a larger inclination angle is released, and the contraction shape occurs more frequently near the keyhole tip instead of at the middle penetration. This result further confirms numerically that the weaker melt convection combined with a smaller keyhole penetration benefits enhanced dynamic stability, as early reported in [36–38].

Figure 15 records the maximum values of temperature, pressure, and velocity magnitude as the simulation proceeds from 62 to 62.4 ms. The values exhibit a drop tendency with the decrease of laser peak power P_L or the increase of welding speed u. The nonlinear variation with higher oscillation amplitude can be more remarkably observed in HF-PLP cases than in CLP cases. Compared to Fig. 11a, b, the valley values of the temperature curves resulted from $P_L = 3800$ W, $u = 0.02$ m/s can be higher than the boiling point of metal due to the thermal accumulation

effect [22], as can be seen in Fig. 15a, b. When P_L reduces to 3300 W, the temperature curves measured in the HF-PLP case intersect with the T_v line during the pulse interval, whereas curves resulting from the CLP condition stay above T_v. This difference also can be found as u increases from 0.02 to 0.03 m/s, providing a quantitative explanation for the variation of vapor eruption characteristics aforementioned in Figs. 13 and 14. Moreover, the poor relationship between the pressure spikes and temperature spikes is more observable under lower heat input conditions, primarily attributed to the less contribution of recoil pressure to the melt acceleration within the weld pool.

4.4 Assessment of prediction accuracy on weld pool dimensions

In Fig. 16, the calculated weld pool depth and width under different heat input modes are demonstrated in relation to welding time. The depth curves calculated in the HF-PLP cases, as summarized in Fig. 16a~c, are relatively lower and more deviated from the experimental measurement than those resulted from the CLP cases. It is mainly attributed to that the averaged heat input of pulsed laser power is much lower than that of continuous laser power, according to Eqs. (1) and (2). Compared to the weld pool depth, less difference can be found with respect to the measurement of molten pool width, as depicted in Fig. 16d~f, in part due to its close correlation to the vapor heating effect which is equivalently implemented by employing a surficial Gaussian heat source at a constant diameter. Considering that the prediction accuracy of using a high-frequency pulse heat source in Q-CLBW simulation has been verified, it can be stated that the modeling scheme coupling with HF-PLP yields higher accuracy in predicting the weld pool dimensions in comparison to that with CLP.

Fig. 13 Temperature, phase, and velocity fields calculated in CLP cases with different laser peak powers and welding speeds
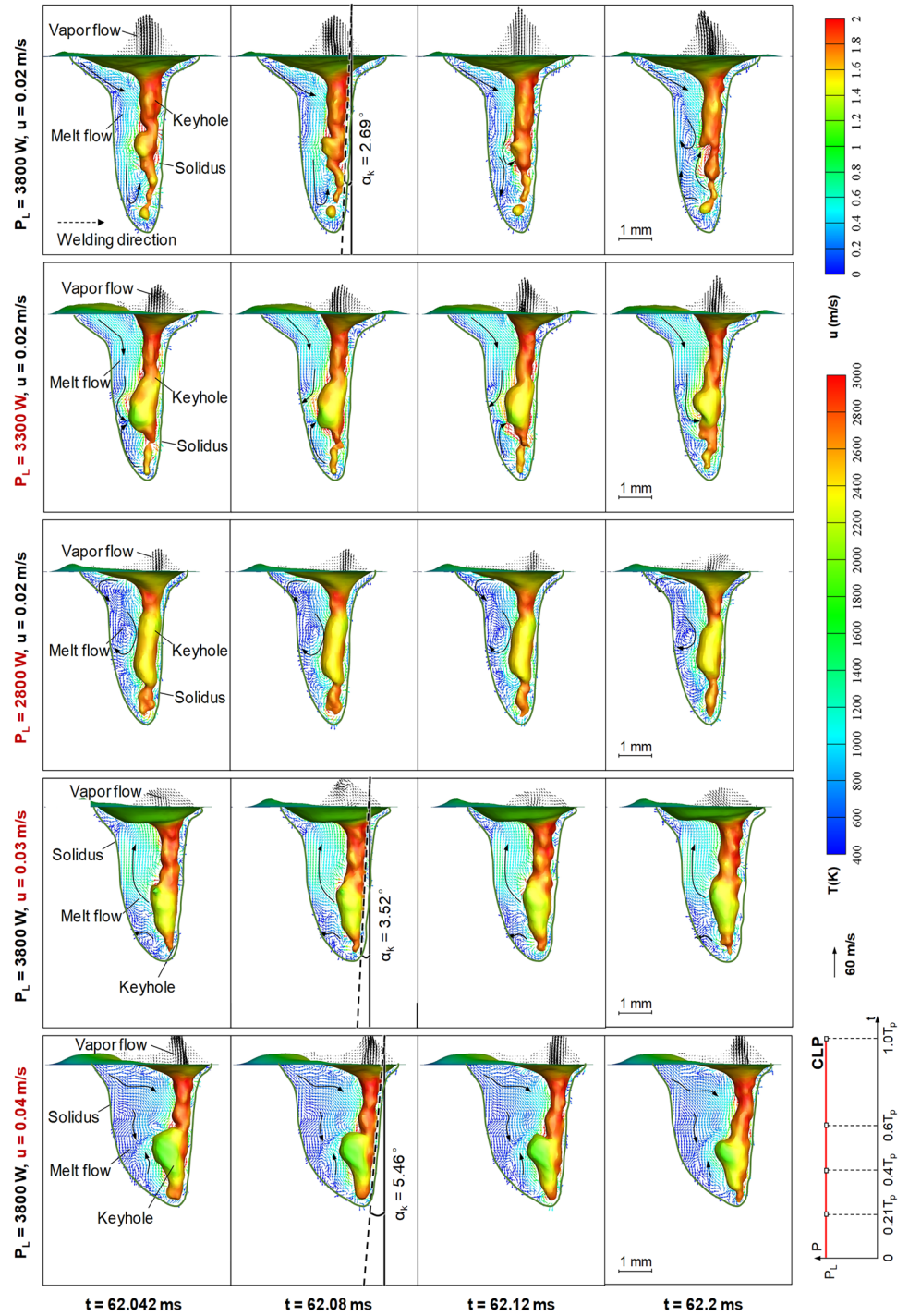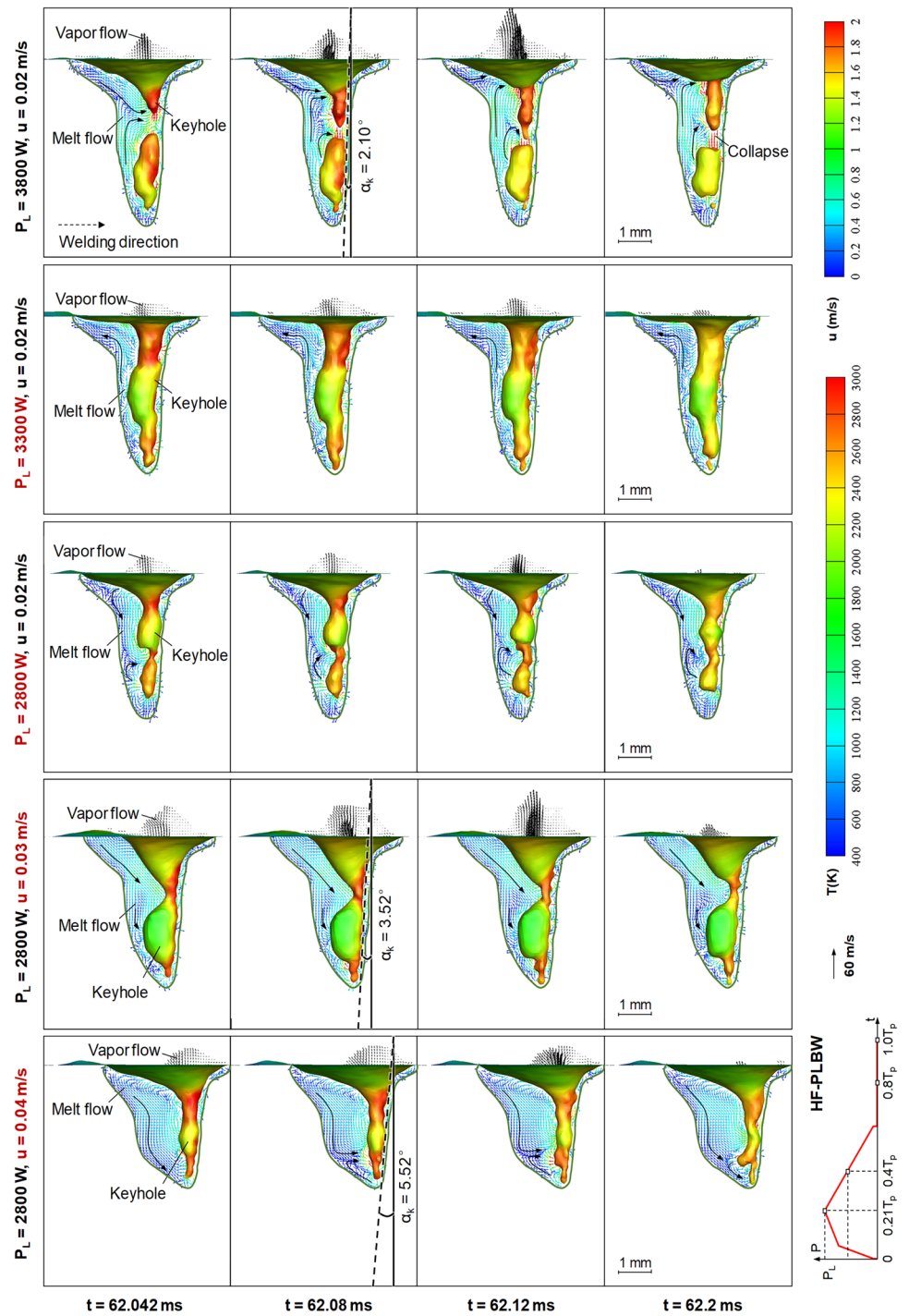
Fig. 14 Temperature, phase, and velocity fields calculated in HF-PLP cases with different laser peak powers and welding speeds
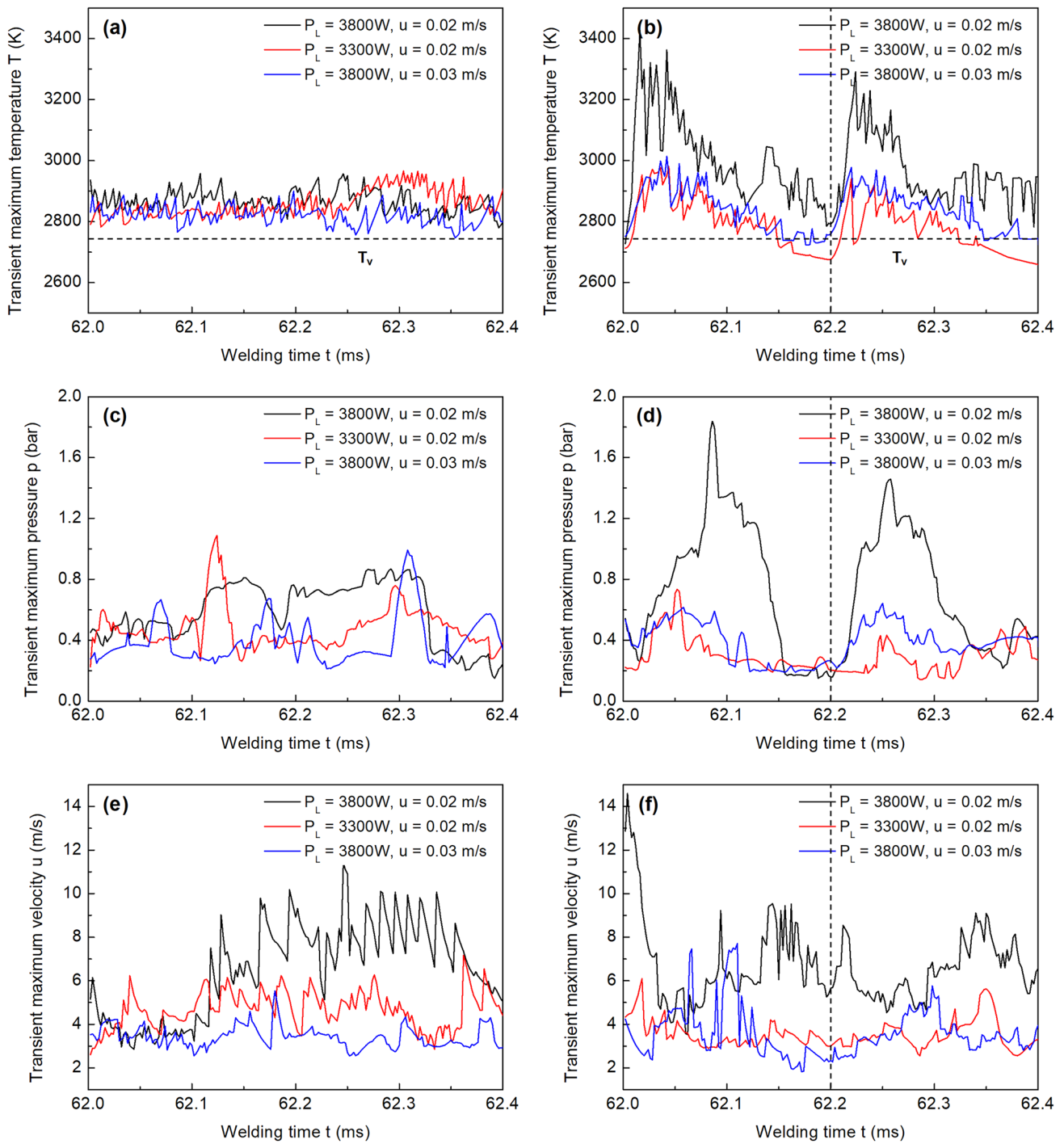
Fig. 15 Measurement of maximum temperature, pressure, and velocity values in relation to welding time: **a** temperature-time curves in CLP cases; **b** temperature-time curves in HF-PLP cases; **c** pressure-time curves in CLP cases; **d** pressure-time curves in HF-PLP cases; **e** velocity magnitude-time curves in CLP cases; **f** velocity magnitude-time curves in HF-PLP cases
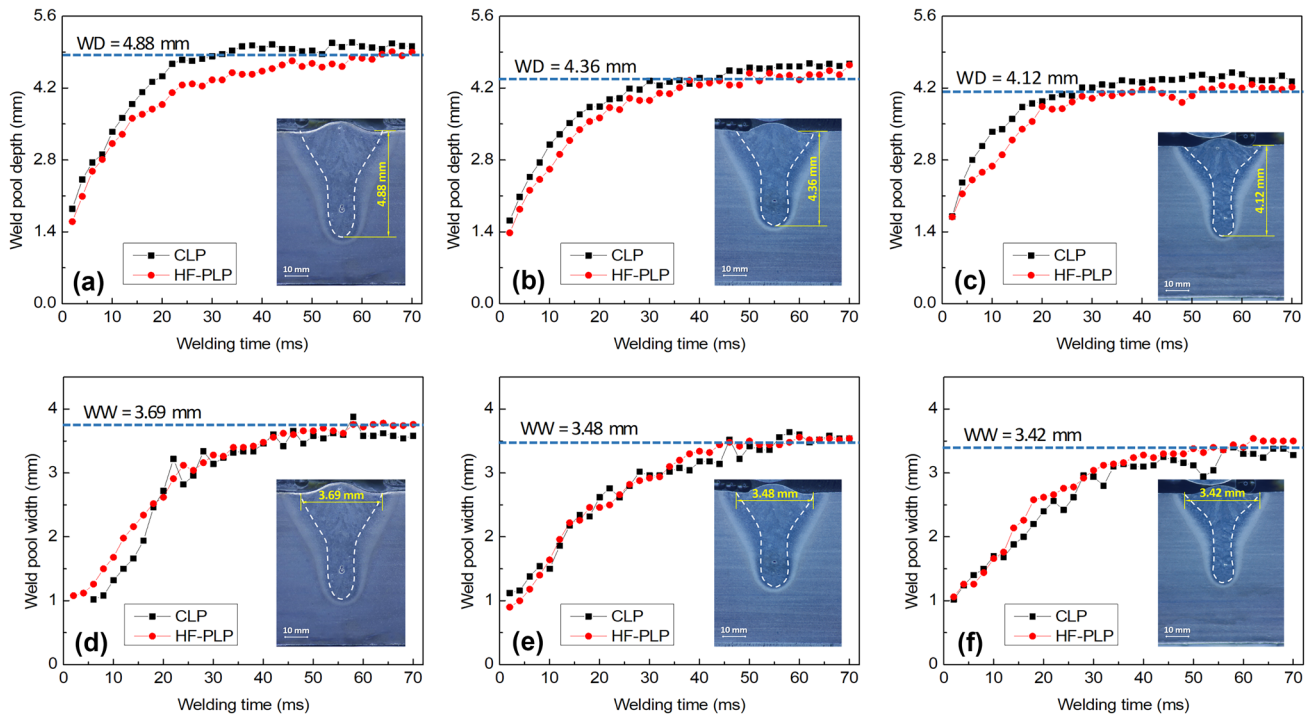
Fig. 16 Measurement of weld pool dimensions in relation to welding time under various heat input: **a** weld pool depth of $P_L = 3800$ W, $u_0 = 0.02$ m/s; **b** weld pool depth of $P_L = 3300$ W, $u_0 = 0.02$ m/s; **c** weld pool depth of $P_L = 3800$ W, $u_0 = 0.03$ m/s; **d** weld pool width of $P_L = 3800$ W, $u_0 = 0.02$ m/s; **e** weld pool width of $P_L = 3300$ W, $u_0 = 0.02$ m/s; **f** weld pool width of $P_L = 3800$ W, $u_0 = 0.03$ m/s

5 Conclusions

This paper proposed a novel and validated numerical model for the CFD calculation of autonomous Q-CLBW on Ti6Al4V alloy plate. A near-reality welding heat input with HF-PLP was employed to simulate the keyhole and weld pool dynamics. The temperature, velocity, and phase fields were compared with those resulting from a conventional heat source with CLP. The difference and deviation with respect to keyhole stability, melt flow pattern, and weld pool dimensions are evaluated qualitatively and quantitatively. Conclusions can be addressed as follows.

1. Compared to the CLP welding cases, the HF-PLP condition yields less stabilized keyhole dynamics featuring with obvious temperature and keyhole morphology fluctuations in each pulse period. The keyhole tends to collapse at the middle depths rather than at the tip segment, resulting in irregular porosity and a remarkable reduction in keyhole depth. The liquid velocity field mainly consists of back-filling flows caused by the imbalance between the recoil pressure and surface tension near the contractions at the keyhole wall. Periodic vapor eruption can be observed above the workpiece.
2. The maximum temperature–time curve of the liquid phase possesses oscillation characteristics in the HF-PLP case, wherein the MOA is much larger than that in the CLP case and the valley values can be lower than the evaporation point, leading to the periodic collapse of keyhole geometry. The pressure spikes are consistent with temperature spikes indicating the dominance of recoil pressure induced by liquid evaporation. The velocity spikes are less correlated to pressure values due to the acceleration or deceleration function of Marangoni shear force during the migration of molten metal.
3. Either the decrease of laser peak power or the increase of welding speed yields higher dynamic stability in HF-PLP cases. A lower heat input stabilizes the molten flow pattern and reduces the keyhole depth, which facilitates a tip-mode collapse of keyhole geometry rather than a middle-depth collapse.
4. The employment of pulsed laser input yields a higher accuracy in predicting the weld pool and seam geometries compared to the results calculated under continuous laser input. HF-PLP rather than CLP should be highly considered in numerical modeling and investigation of the Q-CLBW process.

Author contribution Jicheng Chen: modeling and simulation, data analysis and visualization, writing-original draft preparation and revision. Xiaomei Chen: methodology, experiment, assessment. Xuejun Liu and Yanhong Wei: conceptualization, supervision, writing-reviewing and editing.

Declarations

Ethics approval Not applicable.

Consent to participate The authors declare their consent to participate.

Consent for publication The authors declare their consent for publication.

Conflict of interest The authors declare no competing interests.

References

1. Chang B, Allen C, Blackburn J, Hilton P, Du D (2015) Fluid flow characteristics and porosity behavior in full penetration laser welding of a titanium alloy. Metall Mater Trans B 46:906–918
2. Chen Z, Wang BF, Duan BH (2020) Mechanical properties and microstructure of a high-power laser-welded Ti6Al4V titanium alloy. J Mater Eng Perform 29:2296–2304
3. Seto N, Katayama S, Matsunawa A (2000) High-speed simultaneous observation of plasma and keyhole behavior during high power CO2 laser welding: effect of shielding gas on porosity formation. J Laser Appl 12:245–250
4. Tao W, Yang Z, Chen Y, Li L (2013) Double-sided fiber laser beam welding process of T-joints for aluminum aircraft fuselage panels: filler wire melting behavior, process stability, and their effects on porosity defects. Opt Laser Technol 52:1–9
5. Wolff SJ, Gould B, Parab N, Zhao C, Sun T (2021) Preliminary study on the influence of an external magnetic field on melt pool behavior in laser melting of 4140 steel using in-situ X-ray imaging. J Micro Nano-Manuf 8:041016
6. Yi Z, Chen G, Wei H, Zhang J (2008) A novel "sandwich" method for observation of the keyhole in deep penetration laser welding. Opt Laser Eng 46:133–139
7. Üstündağ Ö, Bakir N, Gumenyuk A, Rethmeier M (2021) Influence of oscillating magnetic field on the keyhole stability in deep penetration laser beam welding. Opt Laser Technol 135:106715
8. Ki H, Mazumder J, Mohanty PS (2002) Modeling of laser keyhole welding: part I. Mathematical modeling, numerical methodology, role of recoil pressure, multiple reflections, and free surface evolution. Metall Mater Trans A 33:1817–1830
9. Ki H, Mazumder J, Mohanty PS (2002) Modeling of laser keyhole welding: part II. simulation of keyhole evolution, velocity, temperature profile, and experimental verification. Metall Mater Trans A 33:1831–1842
10. Cho WI, Na SJ, Thomy C, Vollertsen F (2012) Numerical simulation of molten pool dynamics in high power disk laser welding. J Mater Process Tech 212:262–275
11. Cho WI, Na SJ, Cho MH (2010) Numerical study of alloying element distribution in CO2 laser-GMA hybrid welding. Comp Mater Sci 49:790–800
12. Pang S, Chen L, Zhou J, Yin Y, Chen T (2011) A three-dimensional sharp interface model for self-consistent keyhole and weld pool dynamics in deep penetration laser welding. J Phys D Appl Phys 44:025301
13. Pang S, Chen X, Zhou J, Shao X, Wang C (2015) 3D transient multiphase model for keyhole, vapor plume, and weld pool dynamics in laser welding including the ambient pressure effect. Opt Laser Eng 74:47–58
14. Luo M, Hu R, Li Q, Huang A, Pang S (2019) Physical understanding of keyhole and weld pool dynamics in laser welding under different water pressures. Int J Heat Mass Tran 137:328–336
15. Li Z, Rostam K, Panjehpour A, Akbari M, Rostami S (2020) Experimental and numerical study of temperature field and molten pool dimensions in dissimilar thickness laser welding of Ti6Al4V alloy. J Manuf Process 49:438–446
16. Yang Z, Zhao X, Tao W, Jin C (2019) Effects of keyhole status on melt flow and flow-induced porosity formation during double-sided laser welding of AA6056/AA6156 aluminium alloy T-joint. Opt Laser Technol 109:39–48
17. Chen X, Wei Y, Chang Y, Kong B, Cheng J (2022) Study on keyhole characteristics and weld pool dynamics of Ti6Al4V alloy fabricated by continuous wave laser beam welding. Int J Adv Manuf Tech 119:2999–3012
18. Kumar KS (2015) Numerical modeling and simulation of a butt joint welding of AISI 316l stainless steels using a pulsed laser beam. Mater Today Proc 2:2256–2266
19. Zhou J, Tsai HL, Wang PC (2006) Transport phenomena and keyhole dynamics during pulsed laser welding. J Heat Trans-T ASME 128:680–690
20. Zhou J, Tsai HL (2007) Effects of electromagnetic force on melt flow and porosity prevention in pulsed laser keyhole welding. Int J Heat Mass Tran 50:2217–2235
21. Liang R, Luo Y (2017) Study on weld pool behaviors and ripple formation in dissimilar welding under pulsed laser. Opt Laser Technol 93:1–8
22. Chen J, Ouyang Z, Du X, Wei Y (2022) Weld pool dynamics and joining mechanism in pulse wave laser beam welding of Ti-6Al-4V titanium alloy sheets assembled in butt joint with an air gap. Opt Laser Technol 146:107558
23. Salminen A (2010) The filler wire - laser beam interaction during laser welding with low alloyed steel filler wire. Mechanika 84:67–74
24. Jia Z, Zhang P, Yu Z, Shi H, Tian Y (2020) Effect of pulse shaping on solidification process and crack in 5083 aluminum alloy by pulsed laser welding. Opt Laser Technol 134:106608
25. Gao X, Liu J, Zhang L (2018) Effect of heat input on microstructure and mechanical properties of pulsed laser welded joints in Ti6Al4V/Nb dissimilar alloys. Int J Adv Manuf Tech 94:3937–3947
26. Katayama S, Kawahito Y (2009) Elucidation of phenomena in high-power fiber laser welding and development of prevention procedures of welding defects. Fiber Lasers VI: Technology, Systems, and Applications 7195:71951R
27. Lin R, Wang HP, Lu F, Solomon J, Carlson BE (2017) Numerical study of keyhole dynamics and keyhole-induced porosity formation in remote laser welding of Al alloys. Int J Heat Mass Tran 108:244–256
28. Tan W, Bailey NS, Shin YC (2013) Investigation of keyhole plume and molten pool based on a three-dimensional dynamic model with sharp interface formulation. J Phys D Appl Phys 46:55501
29. Lee WH (1979) A pressure iteration scheme for two-phase flow modeling. Math Model C3:406–4311
30. Norman AF, Ducharme R, Mackwood A, Kapadia P, Prangnell PB (1998) Application of thermal modelling to laser beam welding of aluminium alloys. Sci Technol Weld Joi 3:260–266
31. Qian L, Wei Y, Xiao F (2018) Coupled THINC and level set method: a conservative interface capturing scheme with arbitrary-order surface representations. J Comput Phys 373:284–303
32. Bachmann M, Meng X, Artinov A, Rethmeier M (2022) Elucidation of the bulging effect by an improved ray-tracing algorithm in deep penetration wire feed laser beam welding and its influence on the mixing behavior. Adv Eng Mater 2101299
33. Cho JH, Na SJ (2006) Implementation of real-time multiple reflection and Fresnel absorption of laser beam in keyhole. J Phys D Appl Phys 39:5372–5378

34. Lee JY, Ko SH, Farson DF, Yoo CD (2002) Mechanism of keyhole formation and stability in stationary laser welding. J Phys D Appl Phys 35:1570

35. Ahn J, Chen L, Davies CM, Dear JP (2016) Parametric optimisation and microstructural analysis on high power Yb-fibre laser welding of Ti-6Al-4V. Opt Laser Eng 86:156–171

36. Chen X, Pang S, Shao X, Wang C, Xiao J, Jiang P (2017) Three-dimensional transient thermoelectric currents in deep penetration laser welding of austenite stainless steel. Opt Laser Eng 91:196–205

37. Tan W, Shin YC (2014) Analysis of multi-phase interaction and its effects on keyhole dynamics with a multi-physics numerical model. J Phys D Appl Phys 47:345501

38. Panwisawas C, Perumal B, Ward RM, Turner N, Turner RP, Brooks JW, Basoalto HC (2017) Keyhole formation and thermal fluid flow-induced porosity during laser fusion welding in titanium alloys: experimental and modelling. Acta Mater 126:251–263